remote sensing

MDPI

Technical Note

Atmospheric Optical Characteristics in the Area of 30–400 km

Boris M. Shevtsov *, Andrey N. Perezhogin and Ilya N. Seredkin

Institute of Cosmophysical Research and Radio Wave Propagation, FEB RAS, 7, Mirnaya St., Paratunka, 684034 Kamchatka, Russia

* Correspondence: bshev@ikir.ru

Abstract: Extremely weak lidar reflections in the thermosphere, which correlate with ionosonde data, were detected in 2008 and 2017 over Kamchatka during seasons of low aerosol filling of the atmosphere at solar activity minima. Here, these reflections are considered in comparison with mesospheric and stratospheric lidar signals that makes it possible to determine favorable conditions for thermospheric lidar observations. In 2014, it was shown that lines of transitions between the excited states of atomic nitrogen ions fall within the 532 nm lidar signal emission band, and in 2017, lidar reflections in the thermosphere were simultaneously obtained at 561 and 532 nm excited transitions of atomic oxygen and nitrogen ions, thereby the resonant nature of thermospheric lidar reflections was established and confirmed. Here, using lidar signals at wavelengths of 561 and 532 nm in the altitude range of 30–400 km, by solving the inverse problem, we restore the light scattering coefficients corresponding to these wavelengths that makes it possible to compare the optical characteristics of the thermosphere, mesosphere, and upper stratosphere and to determine the relationship between resonant, Rayleigh, and aerosol light scattering at different heights of the atmosphere. In conclusion, using the scattering coefficients in the thermosphere, we find the cross-sections of light scattering at the 561 and 532 nm transitions of atomic oxygen and nitrogen ions and explain why the scattering coefficients for O^+, 561 nm are less than for N^+, 532 nm, while the concentration of O^+ is two orders of magnitude higher than N^+. The results obtained here are of interest for understanding the ionization effect of solar activity on the optical characteristics of the atmosphere that determine weather and climate changes.

Keywords: optics of the atmosphere; resonant lidar; laser ionozond; lidar reflections in the thermosphere; coefficient and cross-section of light scattering; ionization; aerosol; solar activity; ion aeronomy

check for updates

Citation: Shevtsov, B.M.; Perezhogin, A.N.; Seredkin, I.N. Atmospheric Optical Characteristics in the Area of 30–400 km. *Remote Sens.* **2022**, *14*, 6108. https://doi.org/10.3390/rs14236108

Academic Editor: Michael Obland

Received: 25 August 2022
Accepted: 29 November 2022
Published: 2 December 2022

1. Introduction

The study of the thermosphere is related to the problems of solar activity, space weather, aeronomy, climate, ionization, communications, environment, living systems and much more. The state of the thermosphere depends on the interaction of its gaseous components with solar radiation and fluxes of charged particles. Interactions of the thermosphere with solar radiation can be studied using lidar systems, the frequency selectivity of which is a significant addition to the capabilities of ionosondes. The multi-frequency thermospheric lidar simulates various ranges of the optical spectrum and receives responses from all layers of the atmosphere. This approach is the most adequate in aeronomy. Such systems were proposed long ago [1–9], but thermospheric measurements have appeared only recently [10–13]. Lidar data are essential for space weather modeling and prediction [14–22].

Lidar studies of the thermosphere began with proposals for ${N_2}^+$ [1] and He [2] lidars. However, lidar reflections in the thermosphere were first obtained on N^+ [10,11], and then on O^+ [12]. The correlations of N^+ and O^+ lidar reflections with ionosonde data were studied. Some features of such correlations will be discussed in this article.

Quite recently, lidar reflections in the thermosphere on excited transitions of atomic helium have been obtained [13]. This made it possible to compare two different approaches in lidar studies of the thermosphere. The [13] project uses a narrow-band infrared laser, the neutral component of the thermosphere, and an infrared detector, and the [10–12] project uses a wide-band visible laser, ions, and visible detectors. Infrared lidar technologies have taken longer to implement. In [13], changes in the thermosphere are considered depending on the zenith angle of the sun, and in [10–12], depending on the degree of ionization. With significant technological and methodological differences, one can note the comparability of the lidar signals of the two projects. It can also be noted that these two lidar approaches complement each other well, since they make it possible to carry out aeronomic observations in various ranges of optical radiation with neutral and charged components of the thermosphere. However, most importantly, both projects allow us to work at various altitudes up to a thousand kilometers. Some correlations of lidar signals of the thermosphere and mesosphere will be considered in this article.

However, high sounding heights and weak light scattering in the thermosphere create significant difficulties for the development of lidar methods. The problem is that lidar signals attenuate primarily in the middle and lower layers of the atmosphere, so the problem of thermosphere sounding can be compared to the problem of detecting weak optical reflections through a cloudy screen. This problem cannot be solved simply by increasing the power of the lidar, since it is difficult to detect a weak useful signal after intense exposure of a signal from the lower layers of the atmosphere to the photodetector. Successful sounding of the thermosphere depends on a favorable ratio of light scattering in the upper and lower layers of the atmosphere. Favorable conditions for lidar sounding of the thermosphere will be considered using the example of the ratio of lidar signals from the thermosphere and mesosphere. On days when unfavorable conditions arose in the troposphere and stratosphere, sounding of the thermosphere and mesosphere was not carried out.

With such a strategy of lidar observations, the mesosphere, the aerosol content of which has seasonal and solar cycles, comes to the fore in creating interference. Due to this, the most favorable periods of observations of weak thermospheric lidar reflections arise.

Solar activity simultaneously affects the ionization of the thermosphere and mesosphere, with mesosphere ions becoming the centers of water vapor condensation and water aerosol formation, and in combination, these factors can affect the formation of thermospheric lidar reflections. This is the most probable mechanism for the dependence of thermospheric lidar signals on solar activity. It is obvious that the same ionization mechanism also underlies the aeronomy of the upper layers of the atmosphere, and therefore it is very important to continue lidar observations in the thermosphere in order to understand the mechanisms of the influence of solar activity on climate change.

The features of reflections in the thermosphere are due to their resonant nature. The weakness of the signals is a consequence of the low concentration of scatterers. In this regard, it is necessary to choose the most efficient atomic transitions for light scattering and to determine the optical characteristics of the thermosphere corresponding to these transitions. Below, we will discuss lidar signals of two-frequency sounding of the thermosphere, scattering cross-sections and scattering coefficients of transitions between the excited states of atomic ions of oxygen and nitrogen. The relative efficiency of light scattering on various components of the thermosphere will be determined by comparing the results of two-frequency lidar sounding.

Atomic oxygen dominates in the thermosphere, so it contributes the most to ionization. With this in mind, it is possible to determine the concentration of oxygen ions in the thermosphere from the ionosonde data that makes it possible to verify and calibrate lidar data.

2. Methods and Equipment

Aeronomic studies of the upper layers of the atmosphere require the development of remote methods. Lidar technologies for the study of the thermosphere have been discussed from different points of view [1,2]. Resonant lidars have been proposed to determine the temperature, velocity, and concentrations of metastable He^{1083} [3,4,7–9] and N_2^+ [5] in the thermosphere. Measurements of metastable helium in Earth's atmosphere by resonance lidar are considered in [13].

Here, we consider an alternative solution for thermospheric lidar using a broadband laser. In fact, this is a Rayleigh lidar, which is used in the thermosphere as a resonant one. Surprisingly, this simple solution proved to be successful. It was found from the analysis of lidar observations [10] and then substantiated by [11,12]. The advantage of broadband lidar is the simplicity of the technological solution and the versatility of use at all sounding heights and for various types of scatterers.

In [12], lidar signals at wavelengths of 561 and 532 nm were considered in the range of heights of 100–400 km. Here, we will consider lidar signals in the altitude range of 30–400 km. This allows us to compare the intensity of light scattering at different heights. Using lidar signals, we will determine the scattering coefficients for two wavelengths. This will allow us to find the cross-sections of resonant light scattering on excited ions of atomic oxygen and nitrogen in the thermosphere. The effects of resonant propagation of optical radiation depend on the ratio of these values.

The parameters of the two-frequency Rayleigh lidar with wavelengths of 532 and 561 nm are presented in the Table 1 and Figure 1. This lidar was used in [12]. Transmitter 2 is frequency tunable. The choice of the wavelengths of 532 and 561 nm will be justified below. Until 2017, only transmitter 1 was used. The idea of the two-frequency lidar arose from the understanding of resonant lidar reflections in the thermosphere, after the work [11].

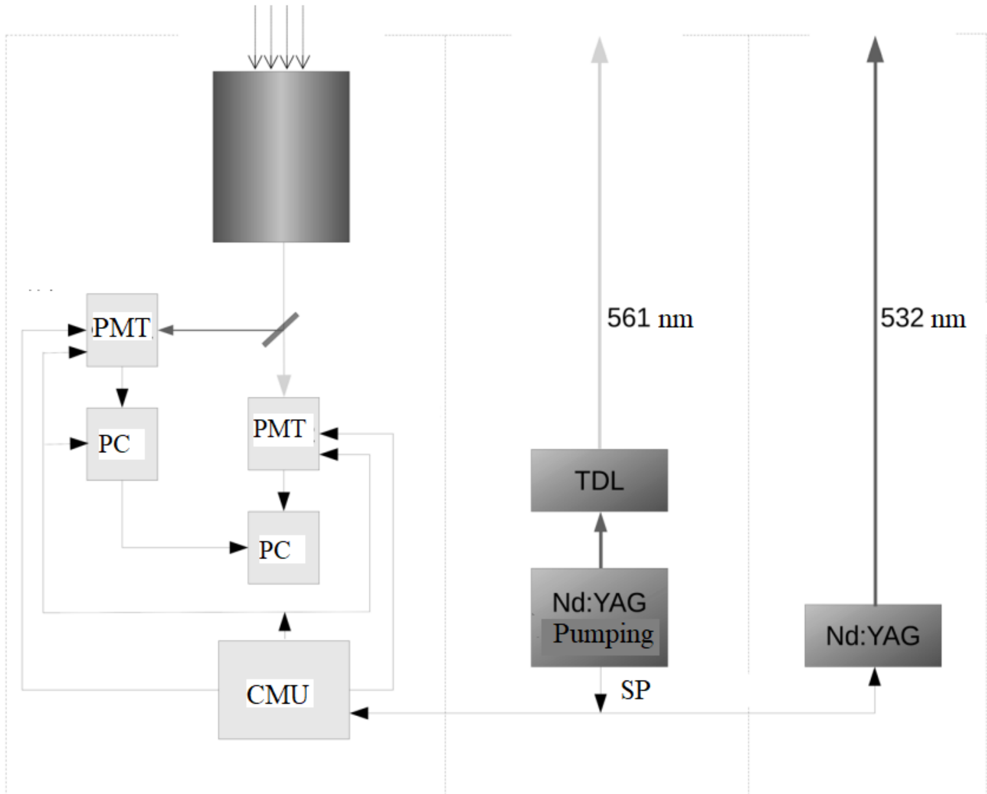

Figure 1. Optical scheme of the lidar. Here, SP—synchro pulse, PC—photon counters, PMT—photomultiplier tubes, CMU—control and monitoring unit.

Table 1. Equipment.

Transmitter 1	Transmitter 2	Receiver
Laser Nd: YAG Brilliant-B Wavelength 532.08 nm Pulse energy 400 mJ Pulse spectrum width 0.040 nm Pulse duration 5 ns Beam divergence 0.5 mrad	Dye laser TDL-90 Pump laser YG-982E Wavelength 561.106 nm Pulse energy 100 mJ Pulse spectrum width 0.025 nm Pulse duration 10 ns Beam divergence 0.5 mrad	Telescope mirror diameter 60 cm Hamamatsu PMT H8259-01 Photon counters M8784-01 Spatial resolution 1.5 km Bandwidth of 1 nm filters

Transitions between excited states of atomic oxygen and nitrogen ions obtained from NIST Atomic Spectra Database [23] are presented in the Table 2. The transition of the nitrogen ion entered into the laser spectrum band with a wavelength of 532 nm by accident [10,11], but the transmitter 2 was specially tuned to the transition of the oxygen ion [12].

Table 2. Transitions of excited ions of oxygen and nitrogen atoms falling into the emission bands of lasers (II—once-ionized atom) [23].

	Component	Wavelength Air (nm)	A_{ki} (s^{-1})	Lower Level	Term	J	Upper Level	Term	J
1	OII	561.1072	2.14×10^6	$2s^2 2p^2(^1S)3s$	^2S	$^1/_2$	$2s^2 2p^2(^3P)4p$	$^2P^\circ$	$^1/_2$
2	NII	532.0958	2.52×10^7	$2s2p^2(^4P)3p$	$^5P^\circ$	1	$2s2p^2(^4P)3d$	^5P	2

In Figure 2, two-wavelength lidar reflections in the thermosphere are presented in comparison with the data of the radio ionosonde [24–26].

The left panel in Figure 2 is the normal case when the lidar signals correlate with the parameters of the ionosphere, and the right panel in Figure 2 is the abnormal case when the lidar signals do not correlate with the ionosonde data. We see two different results on the left and right panels of Figure 2. The second case needs some explanation.

Changes in the lidar signals on 23 September 2017 in Figure 2b were considered in [24,25] as an indicator of the precipitations of charged particles into the atmosphere. However, there was no evidence of precipitations on 23 September 2017, Figure 2d. The ionization of the night thermosphere changed on 23 September 2017 in the usual way. Comparing Figure 2c,d we can see that there were no precipitations on 23 September 2017.

As an alternative to the precipitations, it can be assumed that the cause of the changes in Figure 2b are internal atmospheric oscillations with a period of about two hours. They affect the lidar signals. In [26], it was assumed that strong changes in lidar signals (two orders of magnitude, Figure 2, panel b) were due to changes in the transparency of the underlying layers of the atmosphere. Here, we will show this by comparing lidar signals in the thermosphere and mesosphere, Figures 3 and 4, right panels.

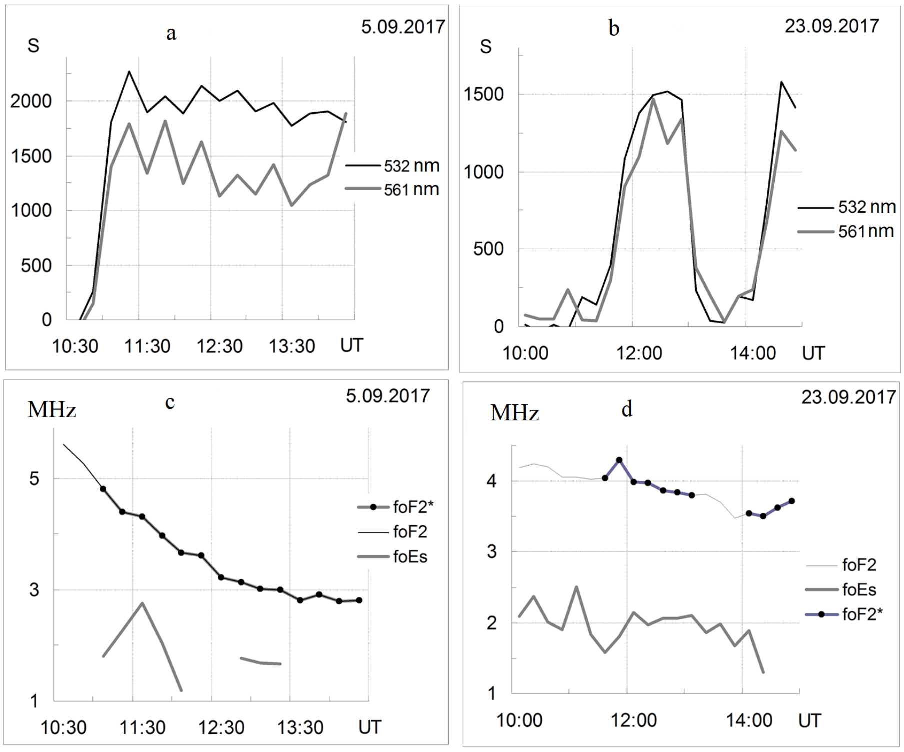

Figure 2. Lidar signals reflected from the layer of 200–400 km (**a**,**b**), and parameters of the ionosphere foF2 and foEs (**c**,**d**) during lidar observations on 5 and 23 September 2017 over Kamchatka.

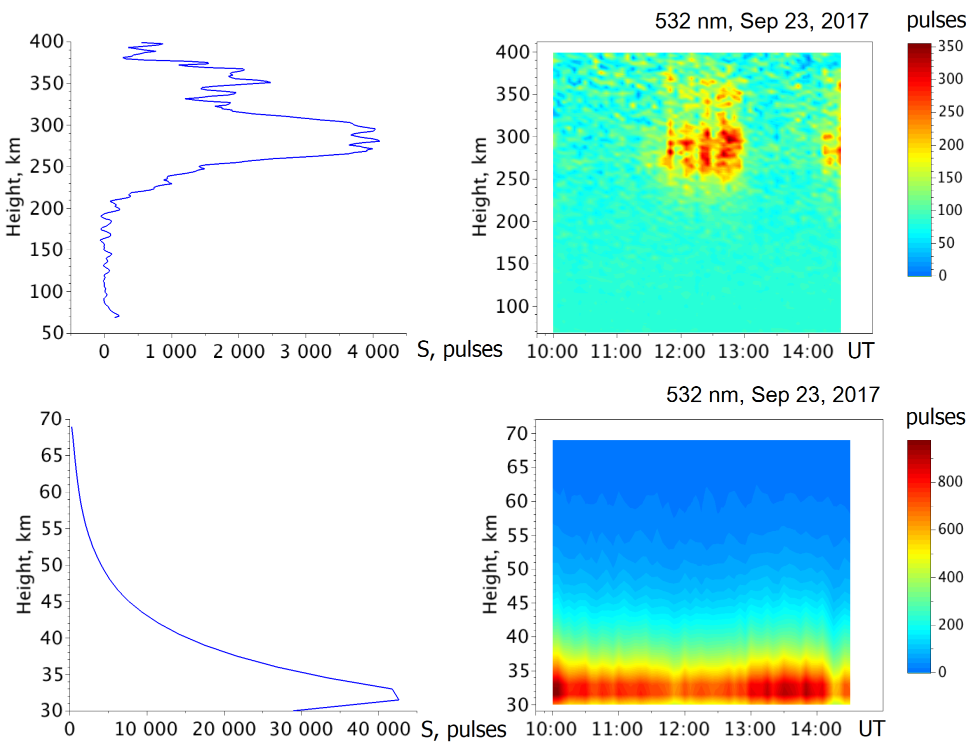

Figure 3. Lidar signal in the thermosphere and mesosphere. The **left** panel shows the lidar signal accumulated over 4.5 h. The **right** panel shows the smoothed lidar signals accumulated every 15 min of 4.5 h. The amplitude of the lidar signal is the number of pulses accumulated in the strobe 1 µs (1.5 km height).

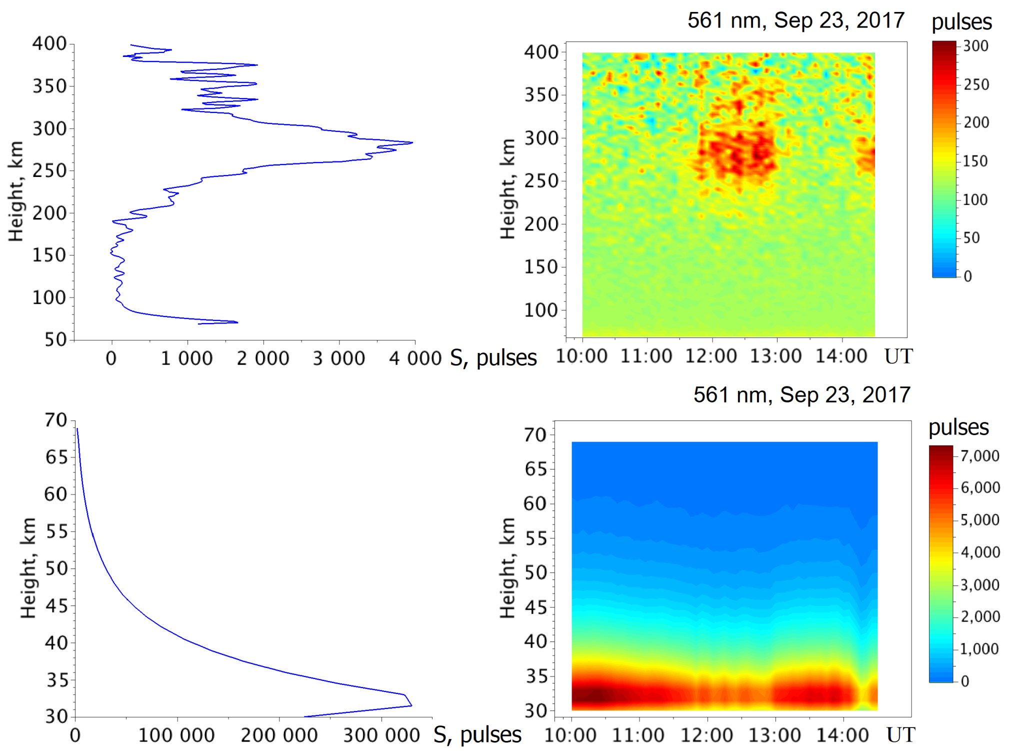

Figure 4. Lidar signal in the thermosphere and mesosphere. The **left** panel shows the lidar signal accumulated over 4.5 h. The **right** panel shows the smoothed lidar signals accumulated every 15 min of 4.5 h. The amplitude of the lidar signal is the number of pulses accumulated in the strobe 1 µs (1.5 km height).

3. Results

3.1. Altitude Profiles of Lidar Signals

Let us consider the lidar signals in the altitude range of 35–400 km. This will allow us to understand how weak thermospheric reflections are relative to scattering in the underlying layers of the atmosphere, and why these reflections are very rarely observed. Essentially, we are dealing with the problem of detecting a weakly reflecting object through a cloudy screen.

Reflections on 23 September 2017 at the wavelength of 561 nm in Figure 4 repeat the features of reflections at the wavelength of 532 nm in Figure 3. Flickering thermospheric reflections occurred between 12 and 13 o'clock when the scattering signals weakened in the mesosphere. The decrease of mesospheric scattering points to the transparency window in the mesosphere that allows us to observe the thermospheric reflections. This corresponds to Figure 2b.

The other situation is illustrated in Figures 5 and 6. Thermospheric reflections on 5 September 2017 lasted for almost the entire observation period, and mesospheric scattering changed little at the wavelength of 532 nm and did not change at wavelength of 561 nm. The left panel in Figure 2 shows that thermospheric reflections on 5 September 2017 correlated with the ionosonde data.

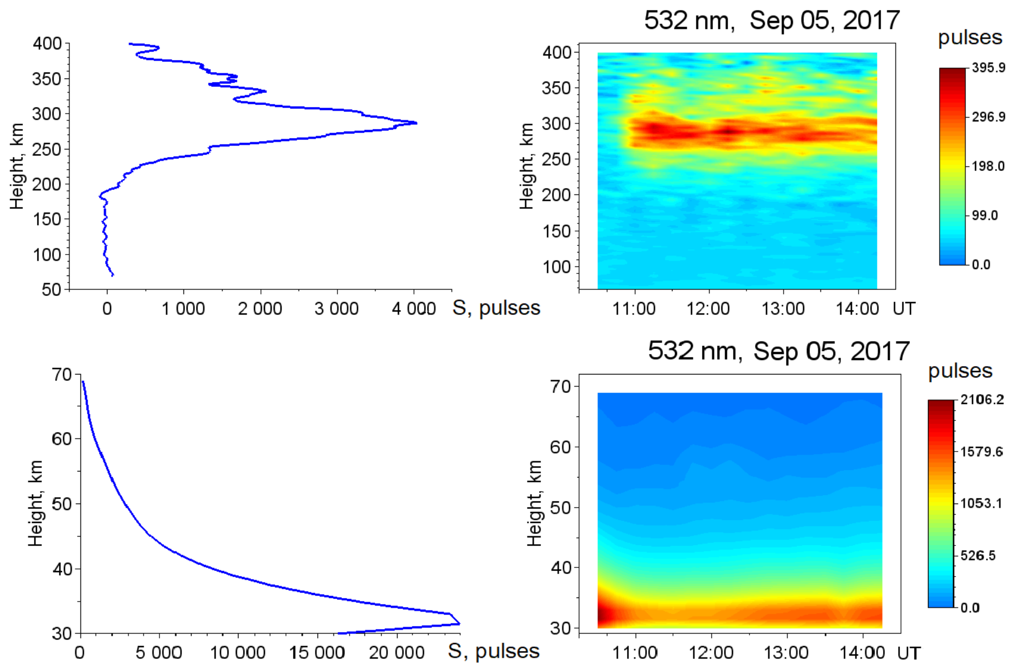

Figure 5. Lidar signal in the thermosphere and mesosphere. The **left** panel shows the lidar signal accumulated over 4.5 h. The **right** panel shows the smoothed lidar signals accumulated every 15 min of 4.5 h. The amplitude of the lidar signal is the number of pulses accumulated in the strobe 1 µs (1.5 km height).

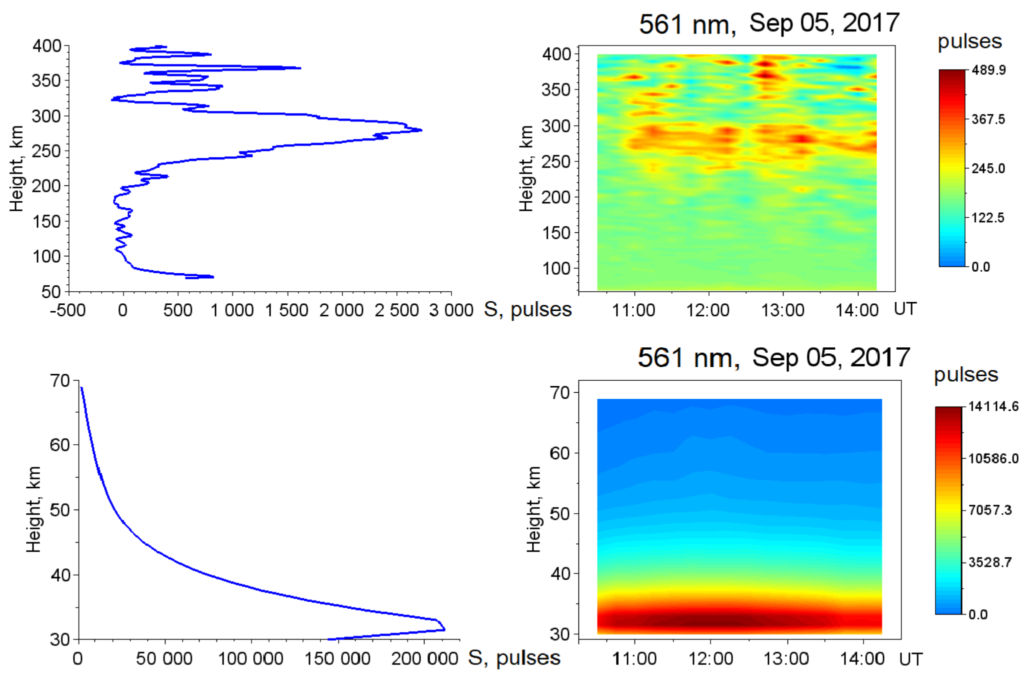

Figure 6. Lidar signal in the thermosphere and mesosphere. The **left** panel shows the lidar signal accumulated over 4.5 h. The **right** panel shows the smoothed lidar signals accumulated every 15 min of 4.5 h. The amplitude of the lidar signal is the number of pulses accumulated in the strobe 1 µs (1.5 km height).

It is possible to draw conclusions from the data presented in Figures 3–6. Thermospheric lidar reflections are formed by the night layer of ions at altitudes of 200–400 km.

The lidar signal from the thermosphere could be received when the transparency of the underlying layer of the atmosphere increased.

The thermospheric lidar reflections correlate with the ionosonde signal and anticorrelate with the lidar signal of the mesosphere.

The most successful thermospheric observations [10,12] were in 2008 and 2017 at the minimum of solar activity during the seasons of low aerosol content of the atmosphere, when weak ionization does not contribute to aerosol formation. This explains the rarity of thermospheric signals.

3.2. Light Scattering Coefficients

Let us consider the coefficients of light scattering in the thermosphere at wavelengths of 561 and 532 nm using lidar signals presented in the left panel of Figures 3–6. Crosslinking of signals in the altitude range of 30–400 km is shown in Figure 7a. Previously, this was conducted at the wave of 532 nm up to the altitude of 150 km [10] that was the beginning of the lidar exploration of the thermosphere.

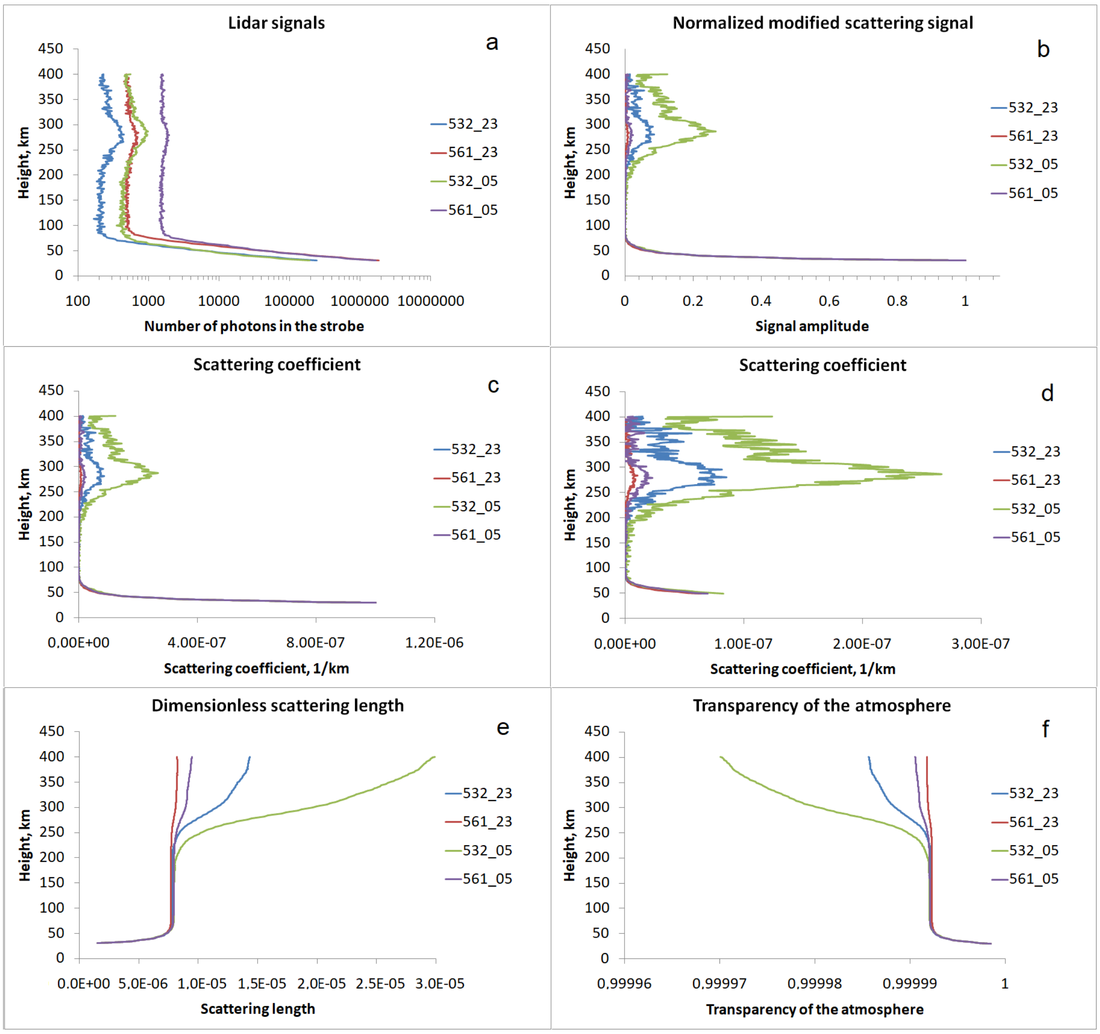

Figure 7. Lidar signals (**a**), normalized modified scattering signals (**b**), scattering coefficients (**c**), scattering coefficients in details (**d**), dimensionless scattering length (**e**) and transparency of the atmosphere (**f**). The legends of the curves indicate the wavelength of the radiation and the day of September 2017.

The constant values of lidar signals in the panel a of Figure 7 show the noise levels, which are the sum of the photoreceiver's dark current and the glow of the night sky. Subtracting noise from the lidar signal gives a scattering signal.

The noise level at a wavelength of 561 nm is greater than at a wavelength of 532 nm in both observations. In both cases, this can be explained by the photoreceiver properties. PMT noise increases with wavelength. Simultaneous variations of the glow of the night sky and the lidar signal in the same spectral range can indicate the precipitation of charged particles, but these correlations were not observed. At the minimum of solar activity, precipitation and the corresponding additional ionization of the F layer of the atmosphere are unlikely.

The height profiles of scattering coefficients $\rho(H)$ were obtained as the inverse solution of the lidar equation $I(H) = (A/H^2)\rho(H)exp(-2\int_h^H \rho(x)dx)$, which describes single scattering.

Using logarithm and differentiation, this integral equation is reduced to a homogeneous Riccati equation (Bernoulli equation), the analytical solution of which is $\rho(H) = (\tilde{I}(H)/\tilde{I}(h))/(1/\rho(h) - 2\int_h^H (\tilde{I}(x)/\tilde{I}(h))dx)$, where $\tilde{I}(H) = I(H)H^2$ (modified scattering signal).

The dimensionless scattering length is calculated as $l = \int_h^H \rho(x)dx$ and the transparency of the atmosphere is $T = exp(-\int_h^H \rho(x)dx)$. The symmetry of Figure 7e,f is a consequence of $l << 1$. This is a criterion for atmospheric transparency, a necessary condition for thermospheric lidar observations.

We observe that the scattering coefficient depends nonlinearly and integrally on the scattering lidar signal. The scattering coefficient $\rho(H) = \sigma \cdot n(H)$, were σ—the scattering cross-section and $n(H)$—the density of scatterers. If the scattering cross-sections σ are known, then the scattering coefficients in Figure 7d give the scatterer densities of N^+ and O^+ in the thermosphere.

3.3. Light Scattering Cross-Sections

Let us estimate the scattering cross-sections of N^+, 532 nm and O^+, 561 nm. In Figure 7d, on 5 September 2017, we have $\rho_{532\text{nm}} = 3 \cdot 10^{-7}$ km^{-1} for N^+ and $\rho_{561\text{nm}} = 3 \cdot 10^{-8}$ km^{-1} for O^+ at the altitude of 300 km.

The density of N at the altitude of 300 km is $n_N = 6 \cdot 10^6$ cm^{-3} and the density of O at the same altitude is $n_O = 6 \cdot 10^8$ cm^{-3} [27].

The density of N^+ at the altitude of 300 km is $n_{N^+} = 3 \cdot 10^3$ cm^{-3} and the density of O^+ at the same altitude is $n_{O^+} = 10^6$ cm^{-3} [28]. Those are daily data. At night, the ionization is an order of magnitude less, so we will use the following values: $n_{N^+} = 3 \cdot 10^2$ cm^{-3} and $n_{O^+} = 10^5$ cm^{-3}.

Next, the populations of the lower and upper levels will be required, Table 1. The populations of energy levels can be estimated as 10^{-4} of the ion concentration [11]: $n_{\tilde{N}^+} = 3 \cdot 10^{-2}$ cm^{-3} and $n_{\tilde{O}^+} = 10$ cm^{-3}.

For the scattering cross-sections, we obtain $\sigma_{532\text{nm}} = 10^{-14}$ m^2 of $\tilde{N}^+$ and $\sigma_{561\text{nm}} = 3 \cdot 10^{-18}$ m^2 of $\tilde{O}^+$. These are rough estimates of the scattering cross-sections. To improve the result, more accurate calculations of the populations of energy levels will be required.

It should be noted that $\sigma_{532\text{nm}}/\sigma_{561\text{nm}} = 3 \cdot 10^3$. To explain this relationship, it is necessary to compare the changes in the electronic configurations of ions N^+ and O^+ in Table 2. They determine the probabilities of inter-level transitions. In the N^+ configuration, we observe an electron transition between 3p and 3d levels with an unchanged electron skeleton, Figure 8. In the O^+ configuration, we observe an electron transition between 3s and 4p levels with the change in electron skeleton between ^1S and ^3P, Figure 9. Of course, a two-electron transition is less likely than a single one. To compare the intensity of transitions, it is also necessary to know the population of energy levels, the assessment of which was discussed above.

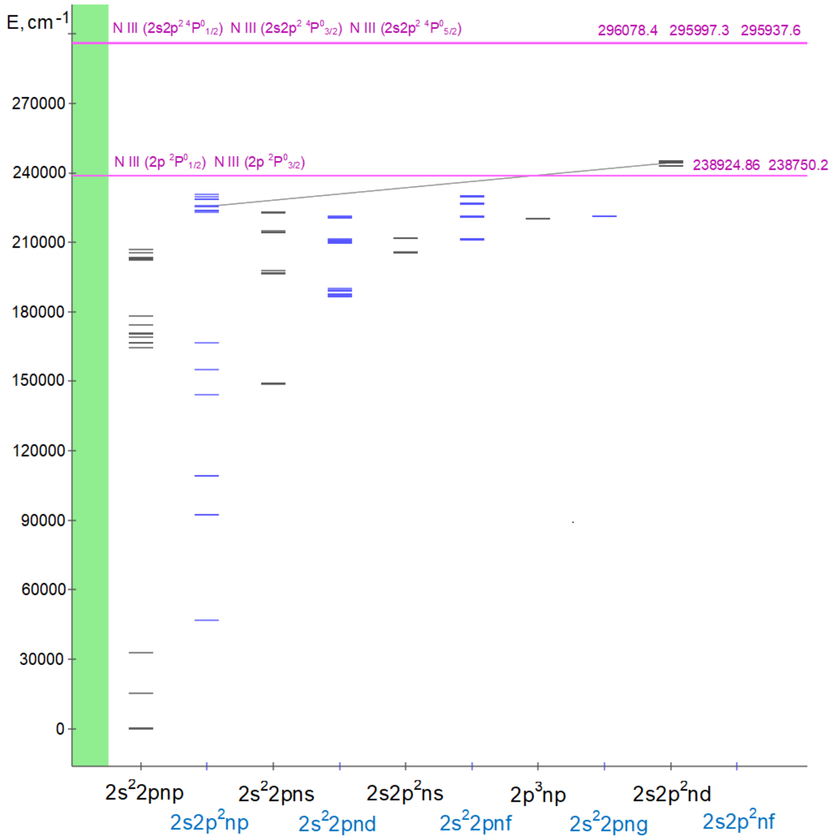

Figure 8. Grotrian diagram of N^{+}, 532 nm.

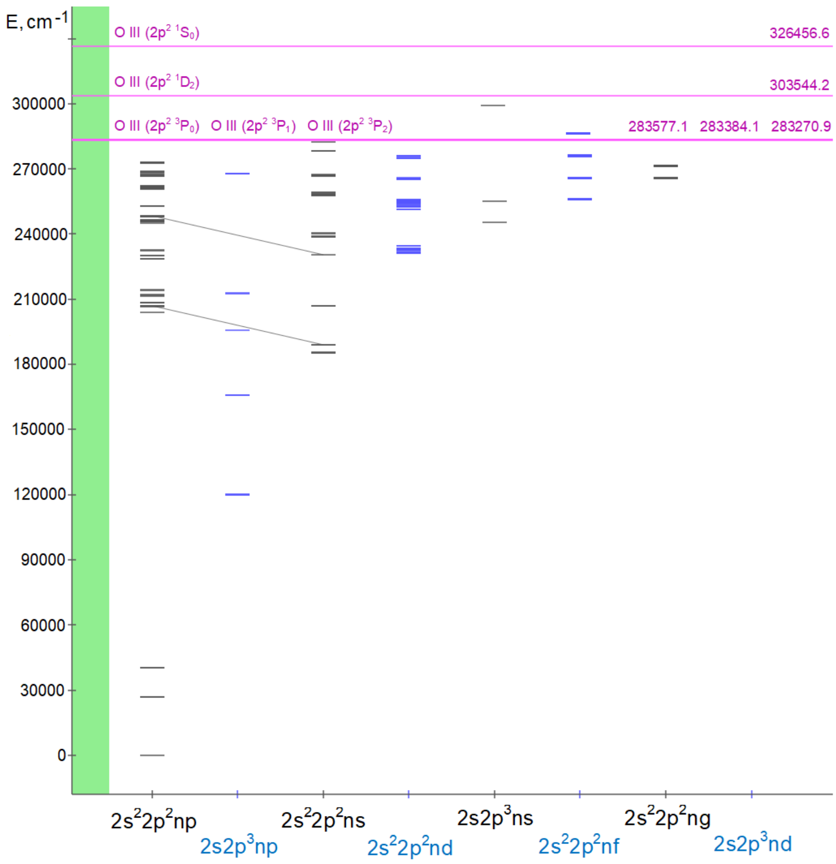

Figure 9. Grotrian diagram of O^{+}, 561 nm.

Due to the small values of the scattering cross-section of O^+ at 561 nm, the lidar signal and the scattering coefficient at 561 nm are smaller than the same parameters at 532 nm, despite the fact that the concentration of O^+ is 2–3 orders of magnitude greater than the concentration of N^+. Therefore, the aeronomic effect of O^+ is less than same effect of N^+.

4. Discussion

Various stages of the development of thermospheric lidar observations are considered, from unexpected detection of resonant scattering in the ionosphere [10] and the study of correlations of lidar reflections with the parameters of the ionospheric F2 layer [11] to multifrequency lidar observations together with radio sounding [12,25]. As a result, a two-channel laser ionosonde is obtained.

Much has been clarified, but some of the results do not have an unambiguous interpretation yet. For example, it is not clear how to distinguish between resonant, Rayleigh and Mi scattering in the middle atmosphere.

The data of He^{1083} thermosphere resonant sounding was obtained [13]. The problem of resonance scattering on neutral components of the thermosphere is solved. He^{1083}, O^+(561 nm) and N^+(532 nm) lidars need to be compared in terms of efficiency.

O and $N_2{}^+$ are still of interest for observation. There is no data of the sounding of the auroral thermosphere during the precipitation of charged particles.

It should be specially noted that H^{1083} is a transition from a metastable state; therefore, an inverse population at the upper level and the resonant propagation of laser radiation can be expected.

The problem of low-noise photodetectors in the IR range creates certain difficulties in the development of IR thermospheric lidars. The solution to this problem was found using superconducting nanowire single-photon detectors [29–31]. The sensitivity of this detector is important when comparing the effectiveness of lidars.

The poor transparency of the atmosphere usually creates great difficulties for high-altitude lidar sounding. There is a need to use satellite ion lidars for sensing the thermosphere. Drones in the sratosphere are of interest for placing thermospheric lidars. At least the strong influence of the transparency of the lower atmosphere that is clearly visible in Figures 3–6 will be excluded.

The concentrations of excited neutral components of the thermosphere are 4–5 orders of magnitude higher than the excited ions discussed above. It is of interest to investigate collective effects in resonant scattering on neutral components of the thermosphere, which may occur with an increase in the concentration of scatterers [32]. The lidar signal on the neutral component of the thermosphere has not yet been received.

The characteristics of resonant light scattering in the thermosphere were obtained using a broadband lidar. With the low efficiency of a broadband laser in resonance sensing, it is easy to adjust its frequency to solve various problems of aeronomy in the thermosphere.

5. Conclusions

The lidar signals from the thermosphere and upper stratosphere are anticorrelated.

The conditions for observing lidar reflections in the thermosphere are significantly determined by the upper stratosphere.

The coefficients of light scattering and scattering cross-sections of N^+, 532 nm and O^+, 561 nm are determined.

The small scattering cross-section of O^+, 561 nm in comparison with the scattering cross-section of N^+, 532 nm is explained by differences in electronic configuration changes.

Author Contributions: Conceptualization, B.M.S.; methodology, I.N.S.; mathematics and software, A.N.P. All authors have read and agreed to the published version of the manuscript.

Funding: The paper was carried out on the subject Physical Processes in the System of Near Space and Geospheres under Solar and Lithospheric Impacts: AAAA-A 21-121011290003-0.

Data Availability Statement: http://www.ikir.ru/ru/CKP (accessed on 24 August 2022), Regulations for user access.

Conflicts of Interest: The authors declare no conflict of interest.

References

1. Collins, R.L.; Lummerzheim, D.; Smith, R.W. Analysis of lidar systems for profiling aurorally-excited molecular species. *Appl. Opt.* **1997**, *36*, 6024–6034. [CrossRef] [PubMed]
2. Gerrard, A.J.; Kane, T.J.; Meisel, D.D.; Thayer, J.P.; Kerr, R.B. Investigation of a resonance lidar for measurement of thermospheric metastable helium. *JASTP* **1997**, *59*, 2023–2035. [CrossRef]
3. Waldrop, L.S.; Kerr, R.B.; Gonzalez, S.A.; Sulzer, M.P.; Noto, J.; Kamalabadi, F. Generation of metastable helium and the 1083 nm emission in the upper thermosphere. *J. Geophs. Res.* **2005**, *110*, A08304. [CrossRef]
4. Chu, X.; Papen, G. *Resonance Fluorescence Lidar for Measurements of the Middle and Upper Atmosphere, 179–432*; Taylor and Francis Group: Abingdon, UK, 2005.
5. Collins, R.L.; Su, L.; Lummerzheim, D.; Doe, R.A. Investigating the Auroral Thermosphere with $N_2{}^+$ Lidar. In *Characterising the Ionosphere. Meeting Proceedings RTO-MP-IST-056, Paper 2*; RTO-MP-IST-056; RTO: Neuilly-sur-Seine, France, 2006; pp. 2-1–2-14. Available online: https://www.researchgate.net/publication/233408410 (accessed on 24 August 2022).
6. Waldrop, L.S.; Kerr, R.; Richards, P. Photoelectron impact excitation of OI 8446 Å emission observed from Arecibo Observatory. *J. Geophys. Res.* **2008**, *113*, 2007JA012356. [CrossRef]
7. Carlson, C.G.; Dragic, P.D.; Graf, B.W.; Price, R.K.; Coleman, J.J.; Swenson, G.R. High power Yb-doped fiber laser-based LIDAR for space weather. In Proceedings of the Lasers and Applications in Science and Engineering, San Jose, CA, USA, 19–24 January 2008; Volume 6873, p. 68730K.
8. Gardner, C.S.; Vargas, F.A. Optimizing three-frequency Na, Fe, and He lidars for measurements of wind, temperature, and species density and the vertical fluxes of heat and constituents. *Appl. Opt.* **2014**, *53*, 4100–4116. [CrossRef]
9. Mangognia, A. Helium Resonance Fluorescence Lidar. Ph.D. Thesis, University of Illinois at Urbana-Champaign, Champaign, IL, USA, 2015.
10. Shevtsov, B.M.; Bychkov, V.V.; Marichev, V.N.; Perezhogin, A.S.; Shumeiko, A.V. Stratospheric aerosol dynamics over Kamchatka and its association with geophysical processes. *Geomagn. Aeron.* **2009**, *49*, 1302–1304. [CrossRef]
11. Bychkov, V.V.; Nepomnyashchiy, Y.A.; Perezhogin, A.S.; Shevtsov, B.M. Lidar returns from the upper atmosphere of Kamchatka for 2008 to 2014 observations. *EPS* **2014**, *66*, 150. [CrossRef]
12. Bychkov, V.V.; Perezhogin, A.S.; Seredkin, I.N.; Shevtsov, B.M. Appearance of light-scattering layers in the thermosphere of Kamchatka during the autumn of 2017. *Proc. SPIE* **2018**, *10833*, 10833A4.
13. Kaifler, B.; Geach, C.; Büdenbender, H.C.; Mezger, A.; Rapp, M. Measurements of metastable helium in Earth's atmosphere by resonance lidar. *Nat. Commun.* **2022**, *13*, 6042. [CrossRef]
14. Akmaev, R.A. Whole atmosphere modeling: Connecting terrestrial and space weather. *Rev. Geophys.* **2011**, *49*, 2011RG000364. [CrossRef]
15. Tao, C.; Jin, H.; Miyoshi, Y.; Shinagawa, H.; Fujiwara, H.; Nishioka, M.; Ishii, M. Numerical forecast of the upper atmosphere and ionosphere using GAIA. *Earth Planets Space* **2020**, *72*, 178. [CrossRef]
16. Heelis, R.A.; Maute, A. Challenges to understanding the Earth's ionosphere and thermosphere. *J. Geophys. Res.* **2020**, *125*, e2019JA027497. [CrossRef]
17. Morley, S.K. Challenges and opportunities in magnetospheric space weather prediction. *J. Space Weather* **2020**, *18*, e2018SW002108. [CrossRef]
18. Hapgood, M. Towards a scientific understanding of the risk from extreme space weather. *Adv. Space Res.* **2011**, *47*, 2059–2072. [CrossRef]
19. Riley, P.; Baker, D.; Liu, Y.D.; Verronen, P.; Singer, H.; Güdel, M. Extreme space weather events: From cradle to grave. *Space Sci. Rev.* **2017**, *214*, 21. [CrossRef]
20. Daglis, I.A.; Chang, L.C.; Dasso, S.; Gopalswamy, N.; Khabarova, O.V.; Kilpua, E.; Lopez, R.; Marsh, D.; Matthes, K.; Nandy, D.; et al. Predictability of variable solar-terrestrial coupling. *Ann. Geophys.* **2021**, *39*, 1013–1035. [CrossRef]
21. Nandy, D. Progress in solar cycle predictions: Sunspot cycles 24–25 in perspective. *Sol. Phys.* **2021**, *296*, 54. [CrossRef]
22. Baker, D.N.; Zurbuchen, T.H.; Anderson, B.J.; Battel, S.J.; Drake, J.F., Jr.; Fisk, L.A.; Geller, M.A.; Gibson, S.; Hesse, M.; Hoeksema, J.T.; et al. *Solar and Space Physics: A Science for a Technological Society*; The National Academies Press: Washington, DC, USA, 2013.
23. Kramida, A.; Ralchenko, Y.; Reader, J.; NIST ASD TEAM. NIST Atomic Spectra Database (Ver. 5.5.2). 2021. Available online: https://physics.nist.gov/asd (accessed on 24 August 2022).
24. Bychkov, V.V.; Perezhogin, A.N.; Seredkin, I.N. Resonant scattering by excited ions as an indicator of the precipitation of charged particles into the atmosphere. *E3S Web Conf.* **2018**, *62*, 01011. [CrossRef]
25. Bychkov, V.V.; Seredkin, I.N. Resonance scattering in the thermosphere as an indicator of superthermal electron precipitation. *Atmos. Ocean. Opt.* **2021**, *34*, 26–33. [CrossRef]
26. Shevtsov, B.M.; Bychkov, V.V.; Perezhogin, A.N.; Seredkin, I.N. Lidar for atmospheric transparency monitoring. *EPJ Web Conf.* **2021**, *254*, 01003. [CrossRef]

27. NRLMSISE-00 Atmosphere Model. 2022. Available online: https://ccmc.gsfc.nasa.gov/modelweb/models/nrlmsise00.php (accessed on 24 August 2022).
28. Richards, P.G. Reexamination of ionospheric photochemistry. *J. Geophys. Res.* **2011**, *116*, A8. [CrossRef]
29. Natarajan, C.M.; Tanner, M.G.; Hadfield, R.H. Superconducting nanowire single-photon detectors: Physics and applications. *Supercond. Sci. Technol.* **2012**, *25*, 063001. [CrossRef]
30. Shangguan, M.; Xia, H.; Wang, C.; Qiu, J.; Lin, S.; Dou, X.; Zhang, Q.; Pan, J.-W. Dual-frequency Doppler lidar for wind detection with a superconducting nanowire single-photon detector. *Opt. Lett.* **2017**, *42*, 3541–3544. [CrossRef] [PubMed]
31. Salvoni, D.; Parlato, L.; Ejrnaes, M.; Mattioli, F.; Gaggero, A.; Martini, F.; Boselli, A.; Sannino, A.; Amoruso, S.; Cristiano, R.; et al. Large area SNSPD for lidar measurements in the infrared. *IEEE Trans. Appl. Supercond.* **2022**, *32*, 1–4. [CrossRef]
32. Andreoli, F.; Gullans, M.J.; High, A.A.; Browaeys, A.; Chang, D.E. Maximum Refractive Index of an Atomic Medium. *Phys. Rev. X* **2021**, *11*, 011026. [CrossRef]